

Article

Arbitrary Sampling Fourier Transform and Its Applications in Magnetic Field Forward Modeling

Shikun Dai ^{1,2}, Ying Zhang ^{1,2,*} , Kun Li ³, Qingrui Chen ^{1,2} and Jiaxuan Ling ^{1,2}

¹ Key Laboratory of Metallogenic Prediction of Nonferrous Metals and Geological Environment Monitoring (Ministry of Education), Central South University, Changsha 410083, China

² School of Geosciences and Info-Physics, Central South University, Changsha 410083, China

³ School of Geoscience and Technology, Southwest Petroleum University, Chengdu 610500, China

* Correspondence: ying.zhang@csu.edu.cn

Abstract: Numerical simulation and inversion imaging are essential in geophysics exploration. Fourier transform plays a vital role in geophysical numerical simulation and inversion imaging, especially in solving partial differential equations. This paper proposes an arbitrary sampling Fourier transform algorithm (AS-FT) based on quadratic interpolation of shape function. Its core idea is to discretize the Fourier transform integral into the sum of finite element integrals. The quadratic shape function represents the function change in each element, and then all element integrals are calculated and accumulated. In this way, the semi-analytical solution of the Fourier oscillation operator in each integral interval can be obtained, and the Fourier transform coefficient can be calculated in advance, so the algorithm has high calculation accuracy and efficiency. Based on the one-dimensional (1D) transform, the two-dimensional (2D) transform is realized by integrating the 1D Fourier transform twice, and the three-dimensional (3D) transform is realized by integrating the 1D Fourier transform three times. The algorithm can sample flexibly according to the distribution of integrated values. The correctness and efficiency of the algorithm are verified by Fourier transform pairs. The AS-FT algorithm is applied to the numerical simulation of magnetic anomalies. The accuracy and efficiency are compared with the standard Fast Fourier transform (standard-FFT) and Gauss Fast Fourier transform (Gauss-FFT). It shows that the AS-FT algorithm has no edge effects and has a higher computational speed. The AS-FT algorithm has good adaptability to continuous medium, weak magnetic catastrophe medium, and strong magnetic catastrophe medium. It can achieve the same as or even higher accuracy than Gauss-FFT through fewer sampling points. The AS-FT algorithm provides a new means for partial differential equation solution in geophysics. It successfully solves the boundary problems, which makes it an efficient and high-precision Fourier transform approach with promising applications. Therefore, the AS-FT algorithm has excellent advantages in solving partial differential equations, providing a new means for solving geophysical forward and inverse problems.

Keywords: arbitrary sample; Fourier transform; numerical simulation of magnetic anomalies; shape-function interpolation



Citation: Dai, S.; Zhang, Y.; Li, K.; Chen, Q.; Ling, J. Arbitrary Sampling Fourier Transform and Its Applications in Magnetic Field Forward Modeling. *Appl. Sci.* **2022**, *12*, 12706. <https://doi.org/10.3390/app122412706>

Academic Editor: Jakub Ciazela

Received: 1 November 2022

Accepted: 6 December 2022

Published: 11 December 2022

Publisher's Note: MDPI stays neutral with regard to jurisdictional claims in published maps and institutional affiliations.



Copyright: © 2022 by the authors. Licensee MDPI, Basel, Switzerland. This article is an open access article distributed under the terms and conditions of the Creative Commons Attribution (CC BY) license (<https://creativecommons.org/licenses/by/4.0/>).

1. Introduction

Fourier transform is an essential tool in the geophysical field, and is of great significance for high-precision numerical simulation and near-surface high-resolution imaging [1–3]. It converts time signals to the frequency domain or spatial signals to the wavenumber domain. It can make fast convolution, target recognition, and other algorithms easy to implement. It is also widely used in waveform analysis, sequence, linear-equation-solving disciplines, and engineering fields [4–6].

In 1965, the release of the Cooley–Tukey fast Fourier transform (FFT) algorithm reduced the complexity of the Fourier transform from $O(N^2)$ to $O(N \log_2(N))$ (where N

represents the scale of the problem), opening up a new field for digital signal processing [7]. Rader proposed that when N is a prime number, DFT calculation can be transformed into cyclic convolution by rearranging the data, which significantly improves the efficiency of the discrete Fourier transform algorithm [8]. Winograd used convolution to calculate DFT, showed a deep correlation between convolution and Fourier transform, and clarified the minimum number of multiple convolutions required for cyclic convolution. The above Fourier transform requires uniform sampling [9]. To realize the Fourier transform algorithm with non-uniform sampling, Dutt and Rokhlin developed a fast Fourier transform algorithm on non-uniform nodes based on the interpolation of the quick multipole method [10]. Beylkin improved the NUFFT algorithm proposed by Dutt and Rokhlin [11]. Subsequently, some scholars conducted further relevant research to improve the accuracy and efficiency of the non-uniform fast Fourier transform (NUFFT) algorithm [12,13]. With the significant improvement of NUFFT algorithm's accuracy and efficiency, a series of NUFFT open-source libraries were proposed accordingly [14–20]. Barnett et al. further optimized NUFFT based on the "semicircular kernel index" and developed a parallel version (FINUFFT), which is significantly more efficient than NUFFT and has the advantage of small memory occupation [21]. The optimized NUFFT algorithm provides a suitable means for numerical problems requiring non-uniform sampling. Fourier transform with uniform or non-uniform sampling provides a good tool for solving many practical problems.

Fourier transform is widely used in geophysical numerical simulation. FFT provides an efficient way to solve geophysical problems, but its edge effects are apparent, affecting data processing [22]. To overcome the edge effects of FFT, Wu and Tian proposed Gauss-FFT technology based on shift sampling [23], which significantly improved the calculation accuracy of FFT and weakened the edge effects, realizing efficient and high-precision calculation of three-dimensional gravity and magnetic field forward modeling [24,25]. Ouyang and Chen applied the Gauss-FFT method to the numerical simulation of a 3D strong magnetic field integral equation. They obtained a high-precision solution using the iterative method, avoiding the influence of zero wavenumbers and improving the forward modeling efficiency [26]. Fan et al. applied non-uniform Fourier transform to electromagnetic scattering problems, which has advantages in solving the issues of non-uniform scatterers and sharp discontinuities [27]. Wu et al. used Gauss-FFT and NUFFT to solve the gravity potential based on the prism model and found that NUFFT solved the singularity problem at zero wavenumbers and had high accuracy [28]. Zhou et al. proposed an FFT algorithm based on cubic spline interpolation that can sample flexibly and apply its results to the forward modeling of gravitational and magnetic potential fields. However, this method's discrete Fourier transform coefficients are related to the values at discrete points. The efficiency is not dominant for the algorithm that needs iteration [29]. Wang et al. applied the NUFFT algorithm based on Gaussian interpolation to 2D gravity numerical simulation and achieved good results [30]. Ouyang et al. applied non-uniform Fourier transform to seismic wave field forward modeling and it performed well [31]. Wang et al. used a 1D NUFFT algorithm for 2D magnetic numerical simulation and the effect was relatively good [32]. However, the efficiency and accuracy of the Fourier transform algorithm can still be improved.

To sum up, standard-FFT is greatly affected by edge effects and spectrum aliasing [33]. Although Gauss-FFT is less affected by edge effects, the total number of wavenumbers increases due to offset sampling, which reduces the computational efficiency, and both algorithms need uniform sampling [26,34]. NUFFT algorithm realizes the non-uniform sampling of the Fourier transform, which is an excellent innovation of Fourier transforms but is still greatly affected by edge effects [32].

To solve these problems, we propose an arbitrary sampling Fourier transform (AS-FT) method based on shape-function interpolation. First, the Fourier transform integral is discretized into the sum of multiple elements, and the original function in each element adopts shape-function interpolation to represent the change. Combined with the kernel in the Fourier transform (natural base exponential function), the semi-analytical solution of

the element integral is obtained. Then all the element integrals are accumulated to obtain the Fourier transform integral. According to the properties of repeated integrals, the 2D Fourier transform integral is realized integrating the 1D Fourier transform twice, and the 3D Fourier transform integral is realized by integrating the 1D Fourier transform three times. In this method, the element can be divided arbitrarily, and it can be divided flexibly according to the trend of the original function. The semi-analytical solution can be obtained using integral element calculation. Because the integral calculation is accurate, there are no edge effects. Flexible sampling is performed according to the integrated function trend, so fewer wavenumbers are selected and the calculation efficiency is higher. Then, the 2D AS-FT algorithm is applied to the 3D weak magnetic and strong magnetic numerical simulation algorithm, and the algorithm’s effectiveness is verified.

2. Methods

The AS-FT method based on shape-function interpolation discretizes the Fourier transform integral into the sum of multiple elements. The function in each element uses shape-function interpolation, obtains the semi-analytical solution of the element integral, and finally adds all the element integrals to the Fourier transform solution. The multi-dimensional Fourier transform is realized by multiply integrating the 1D Fourier transforms.

2.1. 1D AS-FT

One-dimensional Fourier forward transform and inverse transform can be expressed as [35]:

$$\begin{cases} F(k_x) = \int_{-\infty}^{\infty} f(x)e^{-ik_x x} dx \\ f(x) = \frac{1}{2\pi} \int_{-\infty}^{\infty} F(k_x)e^{ik_x x} dk_x \end{cases} \quad (1)$$

where k_x represents the wavenumbers in the direction of x . $f(x)$ is a spatial domain function and $F(k_x)$ is a wavenumber domain function. $f(x)$ and $F(k_x)$ are each other’s Fourier transform functions.

Discretize the forward transform integral in the Equation (1)

$$F(k_x) = \sum_{j=1}^M \int_{e_j} f(x)e^{-ik_x x} dx. \quad (2)$$

where M represents the number of elements and e_j represents the j th element.

The interpolation function of the AS-FT algorithm in this paper can be linear, quadratic, cubic, or higher-order. The higher the degree of the interpolation function, the stronger the ability of a polynomial function to approximate complex function, and the higher the calculation accuracy of the integral is. This section takes quadratic shape-function interpolation as an example to introduce the arbitrary Fourier transform algorithm. A quadratic interpolation shape function is used in the element. Suppose that the coordinates of three nodes in any element are x_1 , x_2 , and x_3 , and x_2 is the midpoint, which meets $x_1 + x_3 = 2x_2$. The nodes in the element are shown in Figure 1:

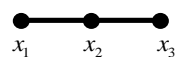


Figure 1. Schematic diagram of elements and nodes in the element.

The values on each node are $f(x_1), f(x_2), f(x_3)$, respectively. $f(x)$ can be expressed by a quadratic shape function [36]

$$f(x) = N_1 f(x_1) + N_2 f(x_2) + N_3 f(x_3), \quad (3)$$

where,

$$\begin{aligned} N_1 &= \frac{(x-x_2)(x-x_3)}{(x_1-x_2)(x_1-x_3)} \\ N_2 &= \frac{(x-x_1)(x-x_3)}{(x_2-x_1)(x_2-x_3)} \\ N_3 &= \frac{(x-x_1)(x-x_2)}{(x_3-x_1)(x_3-x_2)} \end{aligned} \tag{4}$$

Therefore, Equation (2) can be rewritten as

$$F(k_x) = \sum_{j=1}^M \left[\int_{x_1}^{x_3} N_1 f(x_1) e^{-ik_x x} dx + \int_{x_1}^{x_3} N_2 f(x_2) e^{-ik_x x} dx + \int_{x_1}^{x_3} N_3 f(x_3) e^{-ik_x x} dx \right]. \tag{5}$$

Let $W_1 = \int_{x_1}^{x_3} N_1 e^{-ik_x x} dx$, $W_2 = \int_{x_1}^{x_3} N_2 dx$ and $W_3 = \int_{x_1}^{x_3} N_3 e^{-ik_x x} dx$ be the node coefficients of the Fourier transform in the element; then the Equation (5) is abbreviated as

$$F(k_x) = \sum_{j=1}^M [f(x_1)W_1 + f(x_2)W_2 + f(x_3)W_3]. \tag{6}$$

When the wavenumber k_x is not equal to 0, the Fourier transform node coefficients in the element can be obtained by substituting Equation (4); see Appendix A Equations (A1)–(A3) for details.

When the wavenumber k_x is equal to 0, $W_1^0 = \int_{x_1}^{x_3} N_1 dx$, $W_2^0 = \int_{x_1}^{x_3} N_2 dx$, $W_3^0 = \int_{x_1}^{x_3} N_3 dx$ can be integrated to obtain the node coefficient of the Fourier transform at zero wavenumbers as

$$\begin{cases} W_1^0 = \frac{1}{6}(x_3 - x_1) \\ W_2^0 = \frac{2}{3}(x_3 - x_1) \\ W_3^0 = \frac{1}{6}(x_3 - x_1) \end{cases} \tag{7}$$

The final result of the 1D Fourier transform can be obtained by adding up the semi-analytical expressions of different elements. Notably, when the spatial domain and frequency domain partitions are unchanged, the Fourier transform node coefficients W_1 , W_2 , W_3 , W_1^0 , W_2^0 , and W_3^0 are unchanged. Calculating and storing the Fourier transform coefficients in advance can reduce repeated calculations and improve the algorithm’s efficiency, which is also one of the advantages of this algorithm.

In addition, because the forward and inverse transform have the same form, the final expression result of the inverse Fourier transform is similar to the forward transform expression, so it will not be introduced.

2.2. 2D AS-FT

Two-dimensional Fourier forward transform and inverse transform are performed on function $f(x, y)$, respectively [29]:

$$\begin{cases} F(k_x, k_y) = \int_{-\infty}^{\infty} \int_{-\infty}^{\infty} f(x, y) e^{-i(k_x x + k_y y)} dx dy \\ f(x, y) = \frac{1}{4\pi^2} \int_{-\infty}^{\infty} \int_{-\infty}^{\infty} F(k_x, k_y) e^{i(k_x x + k_y y)} dk_x dk_y \end{cases} \tag{8}$$

where k_x and k_y represent the wavenumbers in the direction of x and y . $f(x, y)$ is a spatial domain function and $F(k_x, k_y)$ is a wavenumber domain function. $f(x, y)$ and $F(k_x, k_y)$ are each other’s Fourier transform functions.

For the Fourier transform integral of Equation (8), because the kernel function is continuous in the integral interval, the double integral can be converted into two one-dimensional integrals: first, a one-dimensional integral in the x direction is performed, then a one-dimensional integral in the y direction, and then the 2D Fourier transform is realized.

Taking the forward Fourier transform in Equation (8) as an example, a one-dimensional Fourier transform for the x direction is first made:

$$E_x(k_x, y) = \int_{-\infty}^{\infty} f(x, y) e^{-ik_x x} dx. \tag{9}$$

Then a 1D Fourier transform of the y direction is performed:

$$F(k_x, k_y) = \int_{-\infty}^{\infty} F_x(k_x, y) e^{-ik_y y} dy. \tag{10}$$

The integrals of Equations (9) and (10) above are solved by a 1D Fourier transform. The process of 2D inverse transform is the same as the forward transform, and will not be repeated.

2.3. 3D AS-FT

A three-dimensional Fourier forward transform and inverse transform are performed on function $f(x, y, z)$, respectively:

$$\begin{cases} F(k_x, k_y, k_z) = \int_{-\infty}^{\infty} \int_{-\infty}^{\infty} \int_{-\infty}^{\infty} f(x, y, z) e^{-i(k_x x + k_y y + k_z z)} dx dy dz \\ f(x, y, z) = \frac{1}{8\pi^3} \int_{-\infty}^{\infty} \int_{-\infty}^{\infty} \int_{-\infty}^{\infty} F(k_x, k_y, k_z) e^{i(k_x x + k_y y + k_z z)} dk_x dk_y dk_z \end{cases} \tag{11}$$

where k_x, k_y , and k_z represent the wavenumbers in the directions x, y , and z . $f(x, y, z)$ is a spatial domain function and $F(k_x, k_y, k_z)$ is a wavenumber domain function. $f(x, y, z)$ and $F(k_x, k_y, k_z)$ are each other's Fourier transform functions.

For the Fourier transform integral of Equation (11), similarly, since the kernel function is continuous in the integral interval, the triple integral can be converted into three one-dimensional integrals. First, the x -directional one-dimensional integral is performed, then the y -directional one-dimensional integral on this basis, and finally the z -directional one-dimensional integral, to realize the 3D Fourier transform.

Taking the forward Fourier transform in Equation (11) as an example, first a 1D Fourier transform is performed for the x direction:

$$F_x(k_x, y, z) = \int_{-\infty}^{\infty} f(x, y, z) e^{-ik_x x} dx. \tag{12}$$

Then a 1D Fourier transform of the y direction is performed:

$$F_{xy}(k_x, k_y, z) = \int_{-\infty}^{\infty} F_x(k_x, y, z) e^{-ik_y y} dy. \tag{13}$$

Finally, one-dimensional integration in the z direction is performed on (13) to complete the Fourier transform in the z direction:

$$F(k_x, k_y, k_z) = \int_{-\infty}^{\infty} F_{xy}(k_x, k_y, z) e^{-ik_z z} dz. \tag{14}$$

The integrals of Equations (12)–(14) above are solved by a 1D Fourier transform. The process of the three-dimensional inverse transform is the same as the forward transform, and will not be repeated.

The AS-FT algorithm calculates the Fourier transform coefficients in advance. It can flexibly set the sampling interval according to the distributions of field and spectrum, sparsely, and encrypt the sampling points according to demand. At the same time, the semi-analytical solution of the Fourier oscillation operator can be obtained in the integral interval, which improves the accuracy and efficiency of the Fourier transform.

3. Sampling Rules

The AS-FT method regards Fourier transform as an integral, discretizes the integral, fits the original function with a shape function in each element, obtains the semi-analytical expression of the element, and then obtains the Fourier transform solution. Therefore, the essence of the sampling rule is the fitting degree of the element subdivision to the integrand function. This section uses the quadratic interpolation shape function as an example to introduce arbitrary Fourier transform sampling rules.

3.1. Forward Transform Sampling Rules

The forward transform sampling rules are related to the distribution of the integrand function in the spatial domain. If the function in the spatial domain changes rapidly, the subdivision needs to be encrypted. If the change in the spatial function is relatively gentle, it can be appropriately sparse. Set the space domain sampling interval as Δx_j , the sampling element number as N , and the number of sampling points as $2N + 1$. Set the first sampling point coordinate and the space domain sampling coordinate as x_j

$$\begin{cases} x_{2j-1} = x_0 + j\Delta x_j \\ x_{2j} = x_0 + (j + 1)\Delta x_j \\ x_{2j+1} = x_0 + 2j\Delta x_j \end{cases} \quad j = 1, 2, \dots, N. \tag{15}$$

If the sampling interval is uniform, Δx_j is the fixed value; if the sampling interval is non-uniform, Δx_j will have different values in different intervals. Set the minimum sampling interval as Δx_{min} and the maximum sampling interval as Δx_{max} .

3.2. Inverse Transform Sampling Rules

The inverse transform sampling is related to the distribution of the spectrum. The subdivision is flexible, and it is associated with the sampling in the spatial domain. According to the sampling theorem, the maximum value in the wavenumber domain is

$$k_{max} = \frac{\pi}{\Delta x_{min}}. \tag{16}$$

k_{max} is also the cut-off frequency, and sampling within this cut-off frequency can ensure that all spectrum information can be sampled. When the spectrum changes violently, the maximum wavenumber needs to reach k_{max} . When the spectrum changes slowly and the energy is relatively concentrated, the maximum wavenumber range does not need to reach k_{max} to reduce the number of sampling points to improve the calculation efficiency.

Sampling in the wavenumber domain is divided into uniform sampling and non-uniform sampling. According to the discrete Fourier transform sampling theorem, when sampling uniformly, the wavenumber arrangement is expressed as

$$k_j = p\Delta k, j = 1, 2, \dots, M. \tag{17}$$

where, k_j is the wavenumber arrangement, j is the sequence number of sampling points, Δk is the sampling interval, and M is the sampling points in the wavenumber domain. When the number of sampling points M is even, p is

$$p = -\frac{M}{2}, -\frac{M}{2} + 1, \dots, -1, 0, 1, \dots, \frac{M}{2} - 1. \tag{18}$$

When the number of sampling points M is odd, p is

$$p = -\frac{M-1}{2}, -\frac{M-1}{2} + 1, \dots, -1, 0, 1, \dots, \frac{M-1}{2}. \tag{19}$$

In the case of non-uniform sampling, there are two commonly used methods: piecewise uniform sampling and logarithmic interval uniform sampling. Piecewise uniform sampling is based on uniform subdivisions, encrypted in several intervals where the spectrum changes violently and the energy is strong, and sparse in the intervals where the spectrum changes slowly. Logarithmic interval uniform sampling applies to the spectrum concentration in the region with a small wavenumber and the rapid attenuation of energy as the wavenumber increases, or the energy concentration in the region with a large wavenumber and the rapid attenuation of energy as the wavenumber decreases.

For logarithmic interval sampling, set the wavenumber selection range as $[-k_{max}, k_{max}]$, the number of sampling points in the wavenumber domain as $2M + 1$, and sample uniformly in the logarithmic domain with a sampling interval of

$$\Delta k = \frac{\lg(k_{max}) - \lg(k_{min})}{M} \tag{20}$$

where k_{min} is a small value, generally $10^{-6} \sim 10^{-3}$.

The arrangement of wavenumbers on $[-k_{max}, 0]$ is

$$-k_{max}, \sim -10^{\lg(k_{min})+(M-1)\Delta k} \sim -10^{\lg(k_{min})+(M-2)\Delta k} \sim \dots \sim -10^{\lg(k_{min})+\Delta k} \sim 0. \tag{21}$$

The arrangement of wavenumbers on $[0, k_{max}]$ is

$$0 \sim 10^{\lg(k_{min})+\Delta k} \sim 10^{\lg(k_{min})+2\Delta k} \sim \dots \sim 10^{\lg(k_{min})+(M-1)\Delta k} \sim k_{max}. \tag{22}$$

If some parts of the spectrum change slowly and some parts change violently, uniform and non-uniform sampling can be combined to improve the calculation accuracy and efficiency effectively.

To sum up, forward and inverse Fourier transform sampling rules are mainly based on the change law of the transform function. The sampling with fast energy change is encrypted, and the sampling with slow energy change is sparse. Flexible sampling can consider both calculation accuracy and calculation efficiency.

4. Algorithm Analysis

The algorithm in this paper is written in Fortran95; the development platform is VS2019 under the Windows system, the compiler is IVF2020, and it is carried out on a personal computer with Intel i7 Core 2.3 Ghz and 32 GB RAM.

4.1. Verification of the AS-FT

The simplified Gaussian function verifies the 1D, 2D, and 3D methods of the AS-FT. The spatial domain and wavenumber domain expressions of the Gaussian function are shown in Table 1, where $a = 0.001$. The sampling range of spatial domain x, y, z , and wavenumber domain k_x, k_y, k_z are shown in Table 1. The forward and inverse transform are uniformly sampled, and the number of sampling points is 101.

Table 1. Gaussian function expression and sampling range in spatial domain and wavenumber domain.

	Spatial Domain	Wavenumber Domain	Spatial Domain Sampling	Wavenumber Domain Sampling
1D	$f(x) = e^{-ax^2}$	$F(k_x) = \sqrt{\pi/a}e^{-k_x^2/4a}$	(−100 m, 100 m)	(−0.2, 0.2)
2D	$f(x, y) = e^{-a(x^2+y^2)}$	$F(k_x, k_y) = (\pi/a)e^{-(k_x^2+k_y^2)/4a}$	(−100 m, 100 m)	(−0.2, 0.2)
3D	$f(x, y, z) = e^{-a(x^2+y^2+z^2)}$	$F(k_x, k_y, k_z) = \sqrt{\pi^3/a^3}e^{-(k_x^2+k_y^2+k_z^2)/4a}$	(−100 m, 100 m)	(−0.2, 0.2)

The forward transform result is shown in Figure 2. Compared with the analytical solution, the Relative root mean square (Rrms) error [25] of the 1D forward transform result is 0.012%, the Rrms error of the 2D forward transform result is 0.016%, and the Rrms error of the 3D forward transform result is 0.020%.

The inverse transform result is shown in Figure 3. Compared with the analytical solution, the Rrms error of the 1D inverse transform result is 0.005%, the Rrms error of the 2D inverse transform result is 0.008%, and the Rrms error of the 3D inverse transform result is 0.011%. To sum up, the forward and inverse transform of the AS-FT method has high accuracy.

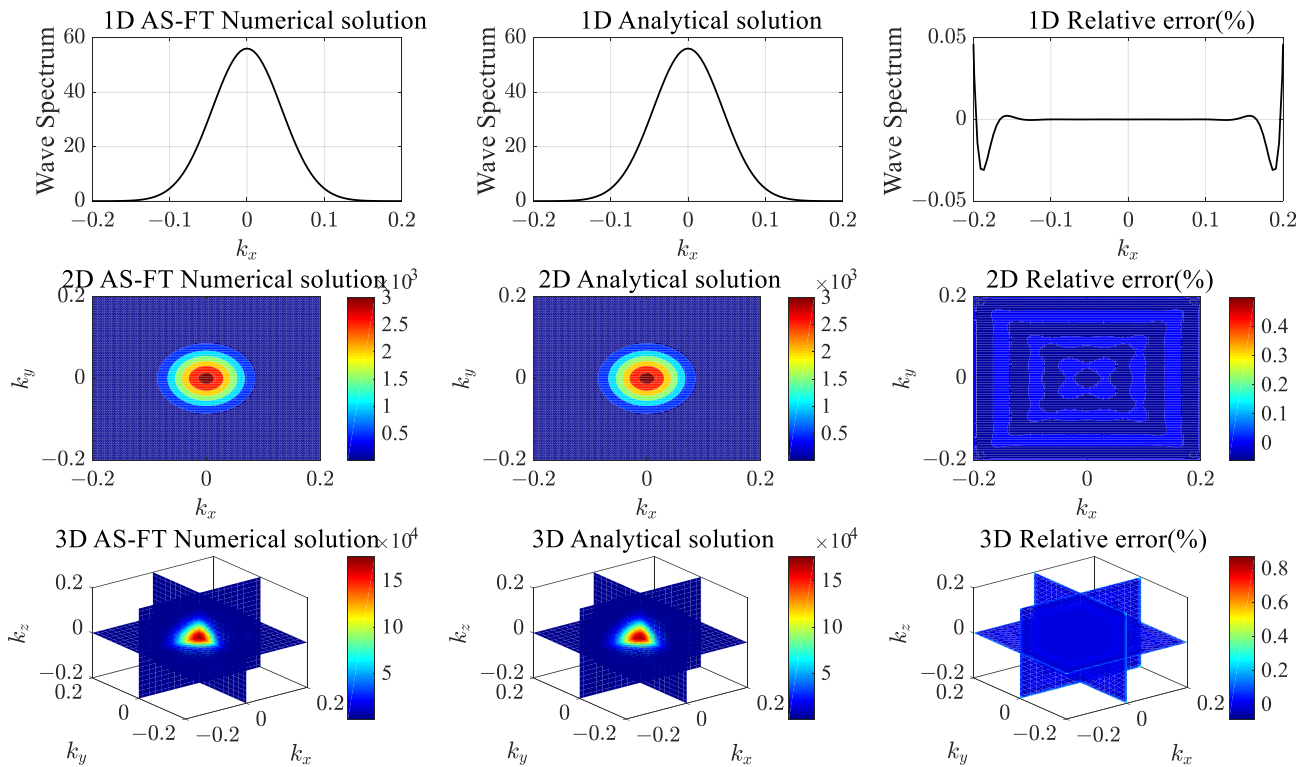


Figure 2. The numerical solution, analytical solution, and relative error of the forward transform.

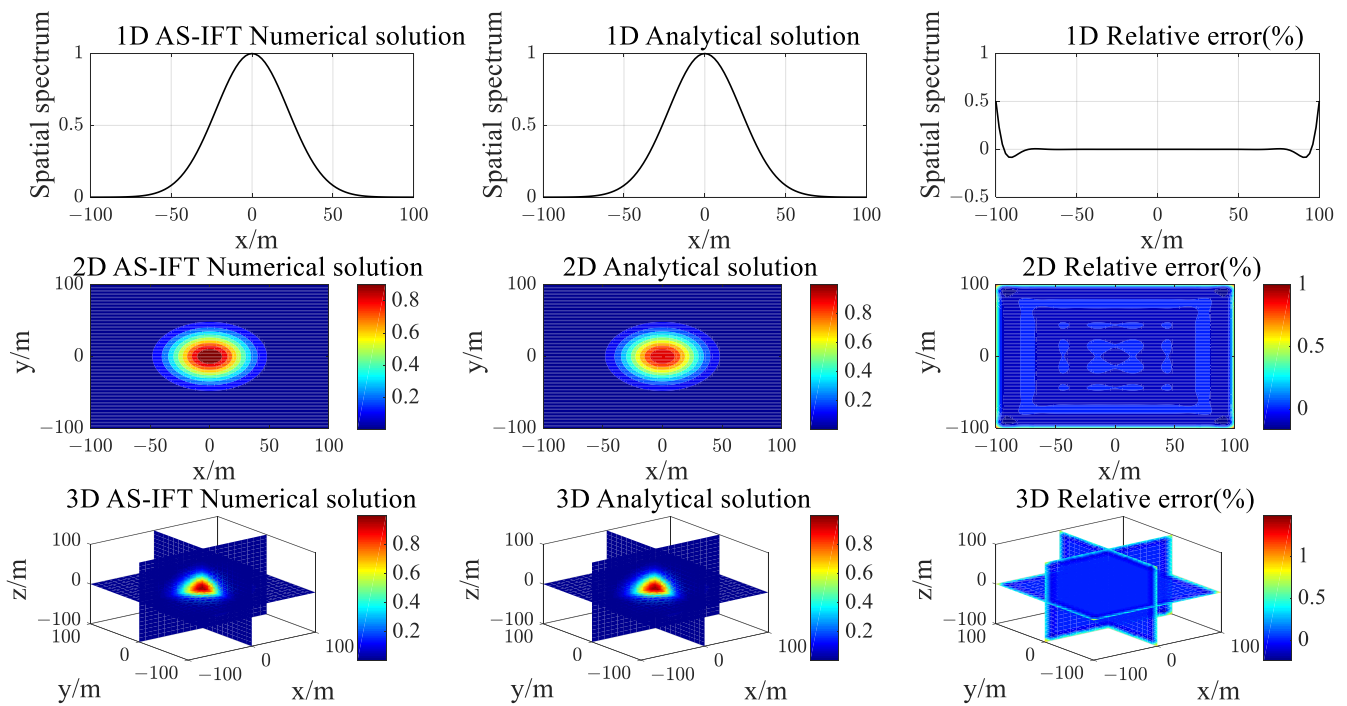


Figure 3. The numerical solution, analytical solution, and relative error of the inverse transform.

4.2. Efficiency Analysis

Based on the Fourier transform pair of the Gaussian distribution function, the time of 1D, 2D, and 3D arbitrary Fourier transform was counted by changing the number of sampling points. Because the forward and inverse Fourier transform algorithms are similar, only the positive transform is taken as an example, and the results are shown in Figure 4.

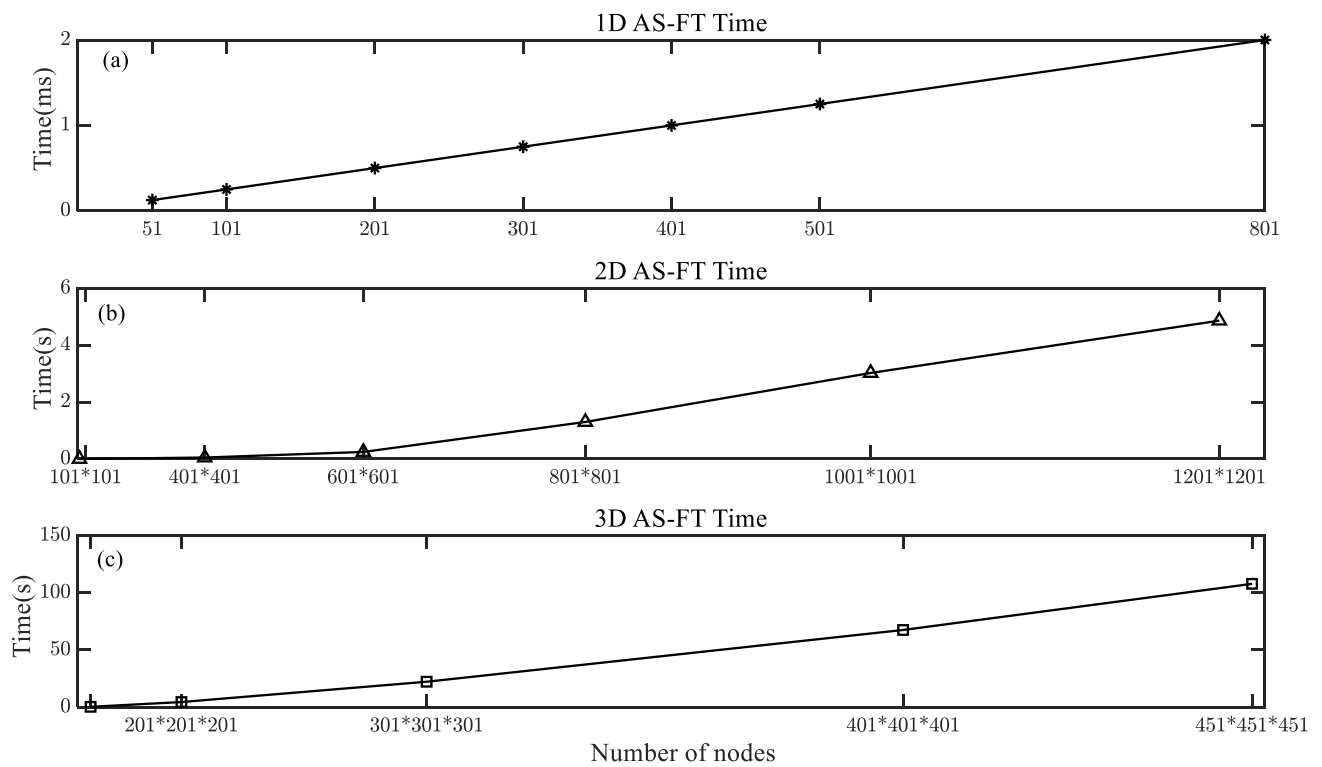


Figure 4. Time required for one transformation of 1D, 2D, and 3D AS-FT. (a) Calculation time of 1D AS-FT under different node numbers. (b) Calculation time of 2D AS-FT under different node numbers. (c) Calculation time of 3D AS-FT under different node numbers.

The number of sampling points in the wavenumber domain is the same as that in the spatial domain. As the number of sampling points in the spatial domain increases, the time required for 1D, 2D, and 3D AS-FT increases linearly, and the algorithm performs well.

5. Results

In this section, the proposed 2D AS-FT algorithm is applied to the 3D space-wavenumber domain numerical simulation of weak and strong magnetic fields in exploration geophysics to test the adaptability and efficiency of the AS-FT algorithm [33,34,37].

5.1. Theory of Magnetic Field Modeling in Space-Wavenumber Domain

The modeling theory of magnetic fields in the space-wavenumber domain reduces the 3D partial differential equation satisfied by the magnetic potential to a 1D ordinary differential equation independent of different wavenumbers by performing a 2D Fourier transform in the horizontal direction that reduces the amount of calculation and storage requirements. The vertical direction is reserved as the spatial domain, and the density of the elements can be adjusted according to the actual situation, which can consider the calculation accuracy and efficiency [37].

The magnetic potential U_a and magnetization \mathbf{M} of the magnetic anomaly field meet the 3D partial differential equation in the spatial domain [38]:

$$\nabla^2 U_a(x, y, z) = \nabla \cdot \mathbf{M}. \tag{23}$$

where (x, y, z) are the coordinates of observation points; ∇^2 is the Laplace operator and $\nabla^2 = \frac{\partial^2}{\partial x^2} + \frac{\partial^2}{\partial y^2} + \frac{\partial^2}{\partial z^2}$; $\nabla \cdot \mathbf{M}$ refers to the divergence of magnetization \mathbf{M} and $\nabla \cdot = \partial/\partial x + \partial/\partial y + \partial/\partial z$.

The magnetization \mathbf{M} is expressed as

$$\mathbf{M} = \chi(\mathbf{H}_0 + \mathbf{H}_a) + \mathbf{J}_r. \quad (24)$$

where \mathbf{H}_0 (A/m) is the background magnetic field, and \mathbf{H}_a (A/m) is the magnetic field of the induction magnetization of the magnetic body, that is, the intensity of the abnormal field. The total field is \mathbf{H} , obtained by $\mathbf{H} = \mathbf{H}_0 + \mathbf{H}_a$. \mathbf{J}_r (A/m) is the residual magnetization.

The horizontal 2D Fourier transform was performed on Equation (23), and a 1D ordinary differential equation was obtained, satisfied by the abnormal magnetic potential in the space-wavenumber domain

$$\frac{\partial^2 \tilde{U}_a}{\partial z^2} - k^2 \tilde{U}_a = ik_x \tilde{M}_x + ik_y \tilde{M}_y + \frac{\partial \tilde{M}_z}{\partial z}. \quad (25)$$

The 1-D FEM was used to solve the above ordinary differential equations. The magnetic field solution can be obtained using the derivative relationship between the magnetic potential and the magnetic field.

It should be pointed out that when the magnetic susceptibility of the abnormal body is less than 0.01 SI, it is a weak magnetic situation, and the abnormal field \mathbf{H}_a can be ignored. The literature [37] analyzes the numerical simulation algorithm of the weak magnetic field in the space-wavenumber domain based on Gauss-FFT and the standard expanded FFT method, which will not be repeated here. The weak magnetic field can be obtained by directly solving Equation (25).

When the magnetic susceptibility of the abnormal body is larger than 0.01 SI, it is a strong magnetic situation, \mathbf{H}_a cannot be ignored, and Equation (25) can be solved by the iterative method [26].

5.2. Efficiency Comparison of Different Fourier Transform Methods

Based on the 3D numerical simulation algorithm of a magnetic anomaly in the space-wavenumber domain [37], the model was designed and simulated by the standard-FFT, Gauss-FFT [24], and AS-FT method proposed in this paper.

The background magnetic field \mathbf{H}_0 is 50,000 nT, the magnetic inclination is 58.3°, and the magnetic declination is 45°. The model is shown in Figure 5.

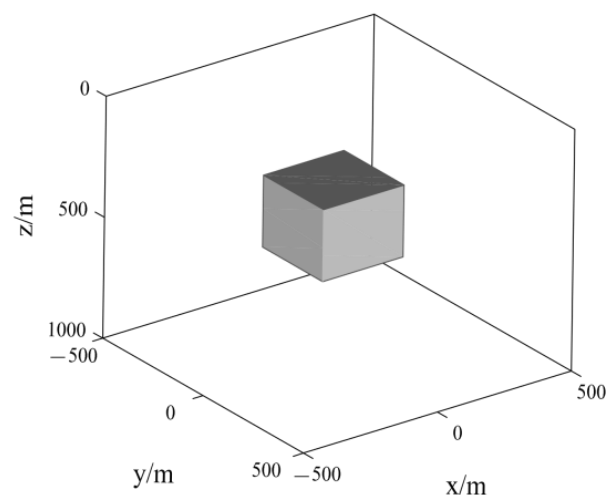


Figure 5. Prism model. The calculation area is 1000 m × 1000 m × 1000 m, with ranges of −500–500 m in the x direction, −500–500 m in the y direction, and 0–1000 m in the z direction. The prism anomaly is a cube with a side length of 400 m, and the prism's center coincides with the model's center. The magnetic susceptibility of the prism is 0.01 SI.

Conditions for comparison of three Fourier transform methods:

- a. K_e is the expansion coefficient of standard-FFT, and the expression is as follows:

$$K_e = \frac{S}{d}, \tag{26}$$

where S refers to the outward expansion distance from the boundary of the simulation area, and d refers to the burial depth of the abnormal body. K_e is taken as 2, 5, and 8, respectively.

- b. The Gauss points of Gauss-FFT are 2, 3, and 4, respectively.
- c. The sampling points in the spatial and wavenumber domains of AS-FT are the same and uniformly sampled.

Gauss-FFT, standard-FFT, and AS-FT algorithms had 101 sampling nodes in the z direction, and the sampling was uniform.

The number of nodes was changed in the horizontal direction, and the efficiency of the three methods and the Rrms error of the ground field value ($z = 0$ m) were compared, as shown in Table 2.

Table 2. Efficiency and accuracy statistics of three Fourier transform algorithms ($N_z = 101$).

Methods	$N_x \times N_y$ or $N_{kx} \times N_{ky}$	N or K_e	Rrms (%)			Time (s)
			B_{ax}	B_{ay}	B_{az}	
Gauss-FFT	201×201	$N = 2$	5.89	5.89	3.95	6.42
		$N = 3$	0.58	0.58	1.32	15.05
		$N = 4$	0.08	0.08	0.24	30.35
Standard-FFT	301×301	$K_e = 2$	1.76	1.76	4.97	2.86
	601×601	$K_e = 5$	0.23	0.23	0.67	11.12
	901×901	$K_e = 8$	0.07	0.07	0.23	39.51
AS-FT	51×51	/	1.21	1.21	1.08	0.14
	101×101	/	0.09	0.09	0.23	0.60
	201×201	/	0.02	0.02	0.11	2.53

According to Table 2, the number of sampling points of Gauss-FFT in the horizontal direction of the spatial domain is 201×201 ; when the Gaussian point in the wavenumber domain is 4, the Rrms of the B_{ax}, B_{ay}, B_{az} reach 0.08%, 0.08%, 0.24%, but it takes 30.35 s. When $K_e = 8$, the accuracy of standard-FFT is the same as that of Gauss-FFT with 4 points, but it takes 39.51 s. When the sample points of spatial and wavenumber domain are 201×201 , the AS-FT algorithm takes only 2.53 s, and the Rrms of B_{ax}, B_{ay}, B_{az} are 0.02%, 0.02%, and 0.11%, respectively.

Therefore, the efficiency and accuracy of the AS-FT algorithm proposed in this paper are better than those of Gauss-FFT and standard-FFT.

5.3. Experiments

The weak magnetic continuum model, weak magnetic catastrophe medium model, and strong catastrophe medium model were designed. Continuous medium and abrupt medium are distinguished by whether the magnetic susceptibility of the abnormal body changes suddenly with the coordinate. The numerical simulation of magnetic anomalies in the space-wavenumber domain based on a 2D AS-FT algorithm was adopted. We tested the applicability of AS-FT to numerical simulation under weak magnetic and strong magnetic conditions, and analyzed the numerical simulation effect of the AS-FT algorithm.

5.3.1. Weak Magnetic Continuous Medium

The continuous medium model was designed a with background magnetic field of 50,000 nT, a magnetic inclination of 45° , and a magnetic declination of 5.9° . The calculation area was $20 \text{ km} \times 20 \text{ km} \times 10 \text{ km}$, with a range of -10 – 10 km in the x direction, -10 – 10 km

in the y direction, and 0–10 km in the z direction. The horizontal magnetic susceptibility changed continuously, and the relationship between magnetic susceptibility and space is shown in Figure 6. The relationship between magnetic susceptibility of the abnormal body and space coordinates is:

$$\chi = 0.02 \times e^{-5 \times 10^{-8} \times (x^2 + y^2)} \text{SI}. \quad (27)$$

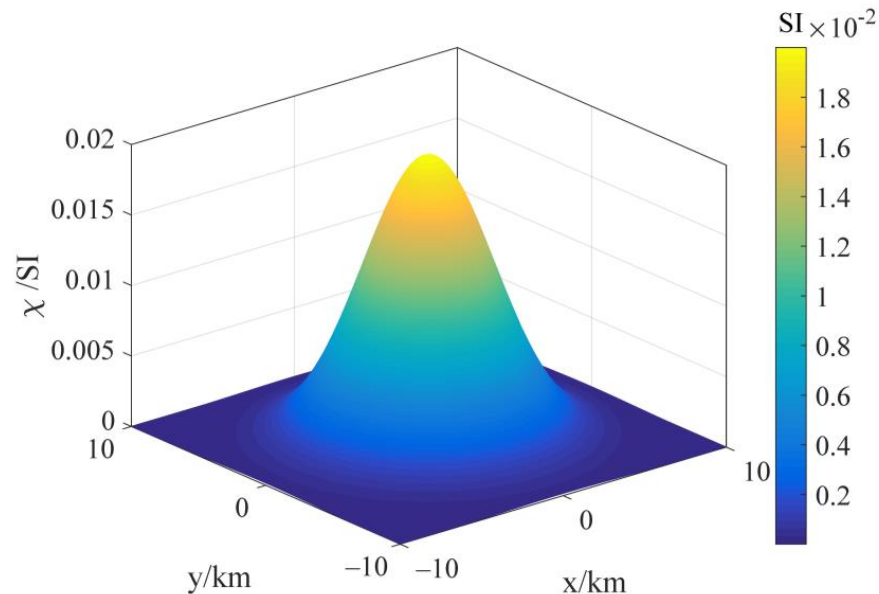


Figure 6. Magnetic susceptibility varying with horizontal coordinates. It represents the magnetic susceptibility change in each layer of the continuous model, and the magnetic susceptibility of different layers is the same.

The x , y , and z directions are sampled uniformly. There were 101 nodes in each direction.

The spectrum distribution of the anomaly field at different depths of the model is shown in Figure 7. By analyzing the spectral distribution of the anomaly field to varying depths of the model and selecting the wave number, the efficiency and accuracy of the numerical simulation can be guaranteed. In Figure 7, the horizontal ordinate adopts non-logarithmic and logarithmic coordinates, and the maximum value is the cut-off frequency, which is obtained according to the sampling theorem. It can be seen that the spectral energy decays to 0 at the cut-off frequency. The spectral energy is different at different depths, but the basic trend is the same.

To analyze the 3D distribution of the spectrum, the distribution of the magnetic anomaly spectrum at the position of $z = 3$ km was taken, as shown in Figure 8. It can be seen through the spectrum distribution that the continuous model spectrum is concentrated, the changing trend is gentle, and there is almost no vibration. To reduce the number of wavenumbers, it is not necessary to sample to the cut-off frequency, which can also ensure the algorithm's accuracy. Combined with Figures 7 and 8, the wavenumber selection range can be set as -1.55×10^{-3} – 1.55×10^{-3} , with uniform sampling.

The numerical simulation results based on Gauss-FFT (4 Gaussian points) with $201 \times 201 \times 101$ sampling points were used as a reference to measure the calculation accuracy of the AS-FT algorithm when different mesh divisions and wavenumbers were selected.

The sampling points in the spatial domain and wavenumber domain were $51 \times 51 \times 101$ and $101 \times 101 \times 101$, respectively, and the samples are uniformly sampled. The accuracy is shown in Table 3. It can be seen that $51 \times 51 \times 101$ nodes achieved high accuracy, and $101 \times 101 \times 101$ nodes achieved higher accuracy.

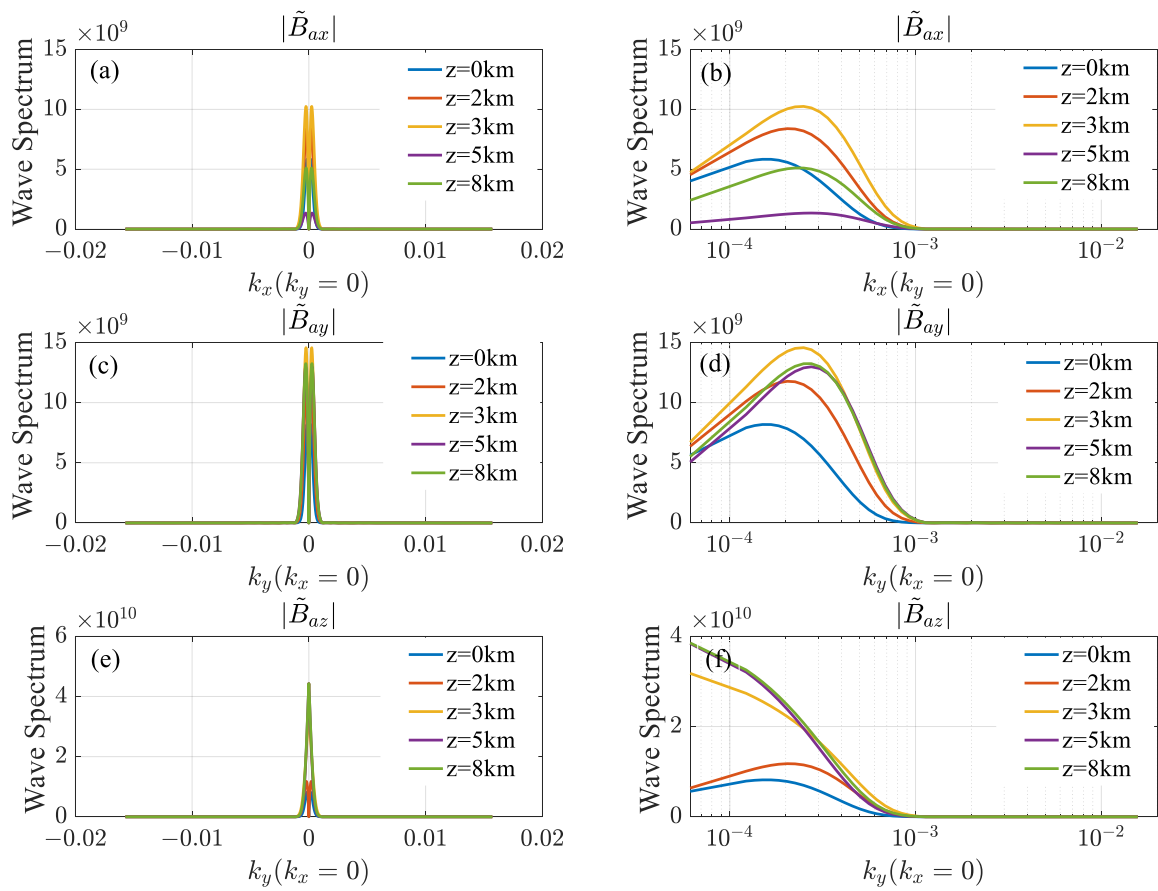


Figure 7. Spectrum distribution of anomaly field at different depths. The horizontal ordinate of figures (a,c,e) is non-logarithmic, and the horizontal ordinate of figures (b,d,f) is logarithmic.

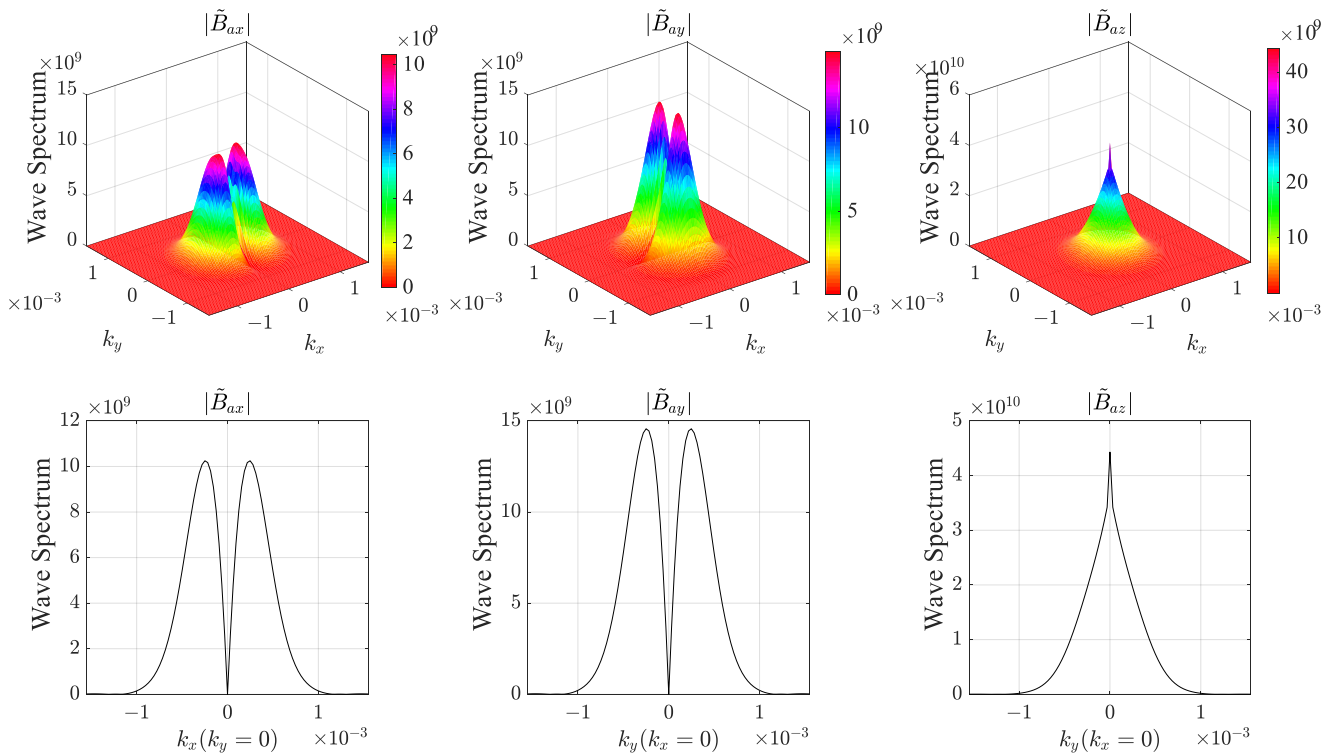


Figure 8. Magnetic field spectrum distribution in wavenumber domain ($z = 3$ km).

Table 3. Accuracy statistics of different sampling points between -1.55×10^{-3} – 1.55×10^{-3} in the wavenumber domain ($z = 0$ m, $N_z = 101$, uniform sampling in both spatial and wavenumber domain).

Number of Sample		Rrms Error (%)		
Spatial Domain $N_x \times N_y$	Wavenumber Domain $N_{kx} \times N_{ky}$	B_{ax}	B_{ay}	B_{az}
51 × 51	51 × 51	0.23	0.73	0.99
101 × 101	101 × 101	0.03	0.06	0.08

When the number of samples was $101 \times 101 \times 101$, the contour map of the numerical solution results of AS-FT and Gauss-FFT are shown in Figure 9. The contour lines are in good agreement, indicating that AS-FT has good adaptability to weak magnetic continuous media. The AS-FT algorithm can achieve higher accuracy with fewer sampling points.

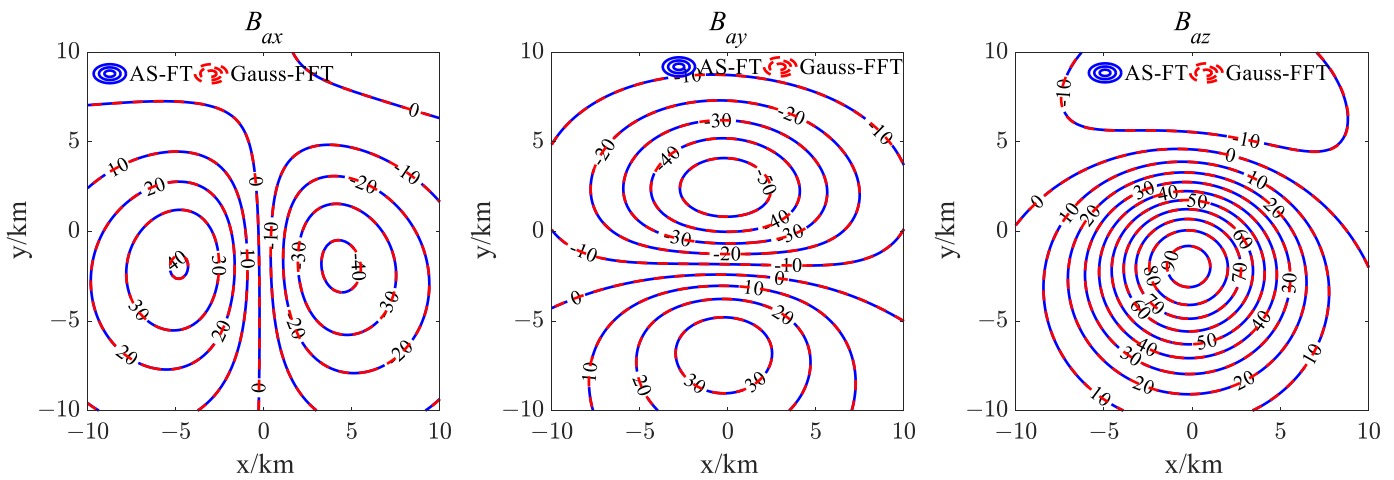


Figure 9. Comparison of continuum model between AS-FT and Gauss-FFT results ($z = 0$ m).

5.3.2. Weak Magnetic Catastrophe Medium

A weak magnetic catastrophe medium model was designed, with a background magnetic field of 50,000 nT, a magnetic inclination of 45° , and a magnetic declination of 5.9° . The model is shown in Figure 10. The x , y , and z directions are sampled uniformly in the spatial domain, and the number of nodes in each of the three directions is 101.

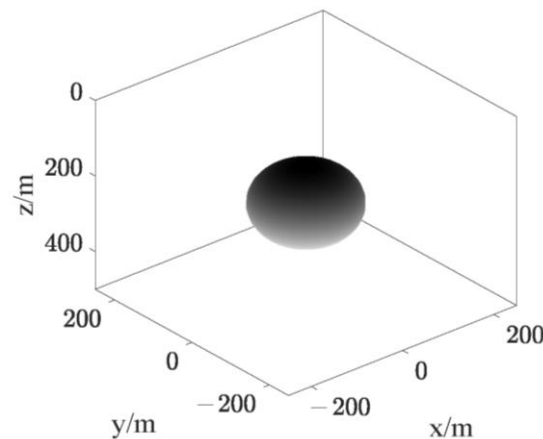


Figure 10. Sphere catastrophe model. The calculation area is $500 \text{ m} \times 500 \text{ m} \times 500 \text{ m}$, with a range of -250 m – 250 m in the x direction, -250 m – 250 m in the y direction, and 0 – 500 m in the z direction. The center of the abnormal sphere model is located at $(0 \text{ m}, 0 \text{ m}, 250 \text{ m})$. The radius of the sphere is 100 m . The magnetic susceptibility of the sphere is 0.01 SI .

The spectrum distribution of the anomaly field at different depths of the model is shown in Figure 11. Since the abnormal body is in the center, the spectral distribution of the abnormal field obtained by numerical simulation is symmetrical about $z = 250$ m, so the spectral distribution of $z = 0$ m, 100 m, 200 m, and 250 m planes was taken for analysis. Compared with the spectral distribution in Figure 7 of the continuous model, the concentration of the spectrum becomes weaker, and the spectrum oscillates at large wavenumbers but attenuates to 0 at the cut-off frequency.

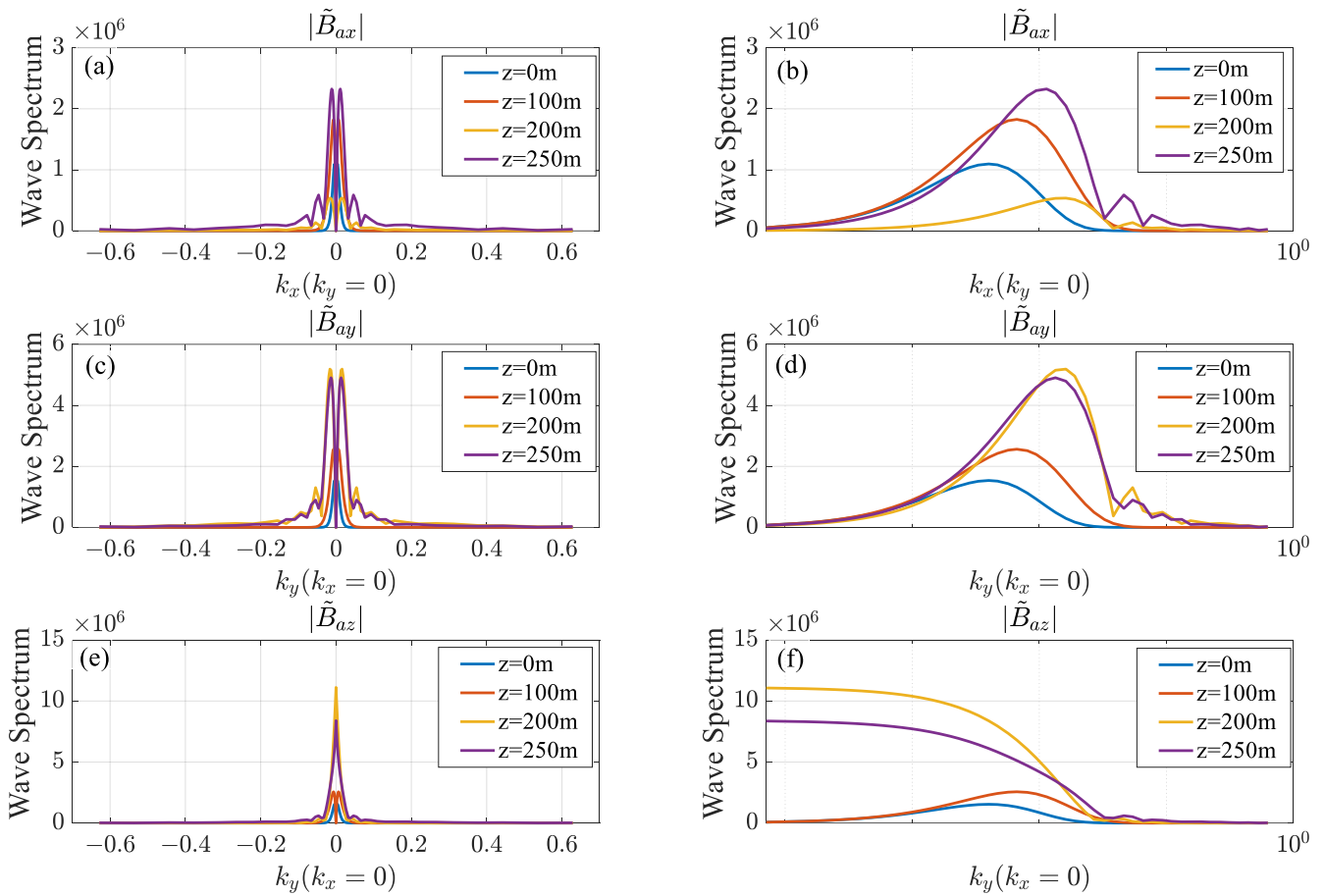


Figure 11. Spectrum distribution of weak magnetic field at different depths. The horizontal ordinate of figures (a,c,e) is non-logarithmic, and the horizontal ordinate of figures (b,d,f) is logarithmic.

To understand the 3D spectrum, the distribution of the magnetic anomaly spectrum at the position of $z = 250$ m is shown in Figure 12. According to the distribution of the spectrum, the distribution of the weak magnetic catastrophe model spectrum is relatively concentrated. Still, with the increase in the wavenumber, the distribution of the spectrum fluctuates slightly. Considering the efficiency and accuracy, the wavenumber selection range is set as $-0.1-0.1$.

The following tests analyzed the influence of uniform and log-domain uniform sampling on the accuracy. It can be seen from Table 4 that the samples are uniformly sampled in the range of $-0.1-0.1$, and the Rrms errors of the ground $z = 0$ m plane B_{ax}, B_{ay}, B_{az} are 0.11%, 0.17%, and 0.22%, respectively. The samples are uniformly sampled in the log domain of $-0.1-0.1$, and the Rrms errors of the ground $z = 0$ m plane B_{ax}, B_{ay}, B_{az} are 0.05%, 0.05%, and 0.06%, respectively.

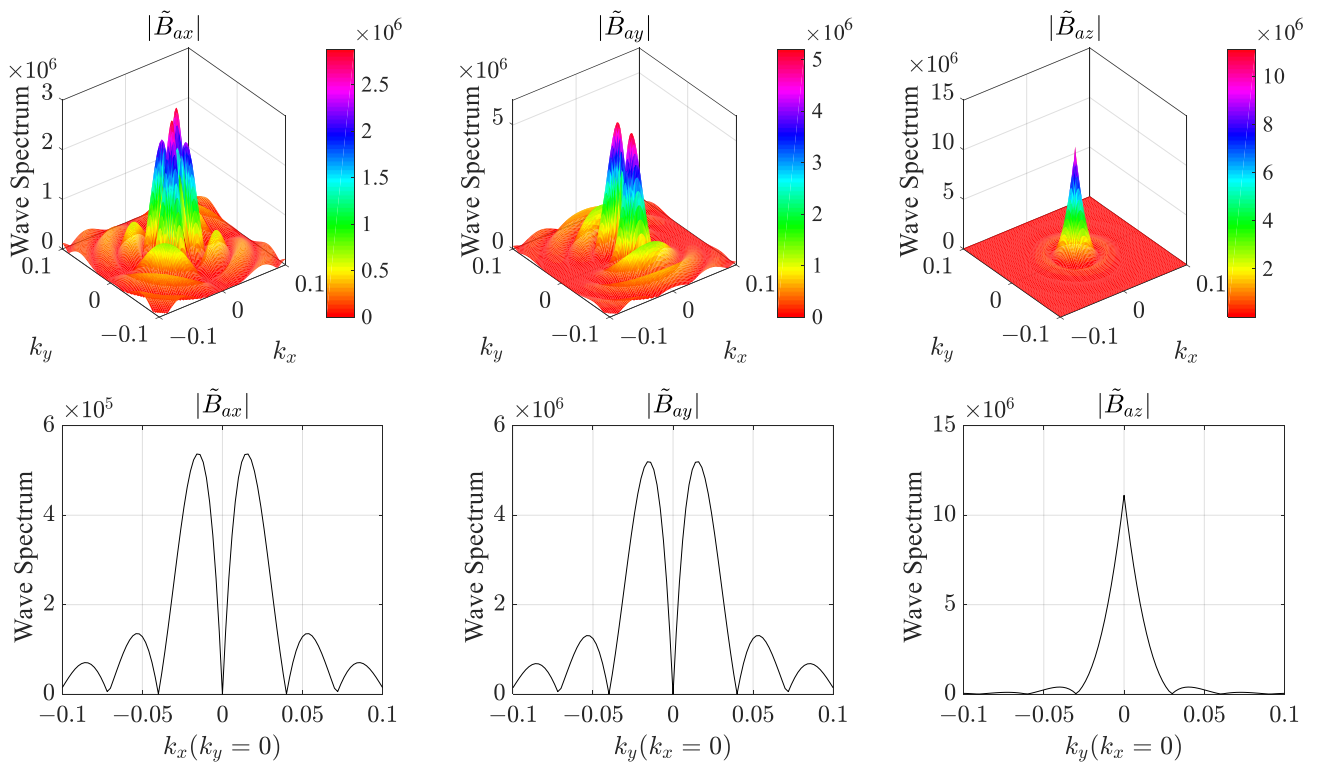


Figure 12. Spectral distribution of weak magnetic field in wavenumber domain ($z = 250$ m).

Table 4. Accuracy statistics of different sampling points between -0.1 and 0.1 in the wavenumber domain ($z = 0$ m, $N_x = N_y = N_z = 101$, $N_{kx} = N_{ky} = 101$).

Wavenumber Domain Sampling Methods	Rrms Error (%)		
	B_{ax}	B_{ay}	B_{az}
Uniform	0.11	0.17	0.22
Log-domain uniform	0.05	0.05	0.06

The comparison between the numerical simulation results of log-domain sampling and the analytical solution of the sphere is shown in Figure 13. The results show that the AS-FT algorithm has high calculation accuracy for the catastrophe model.

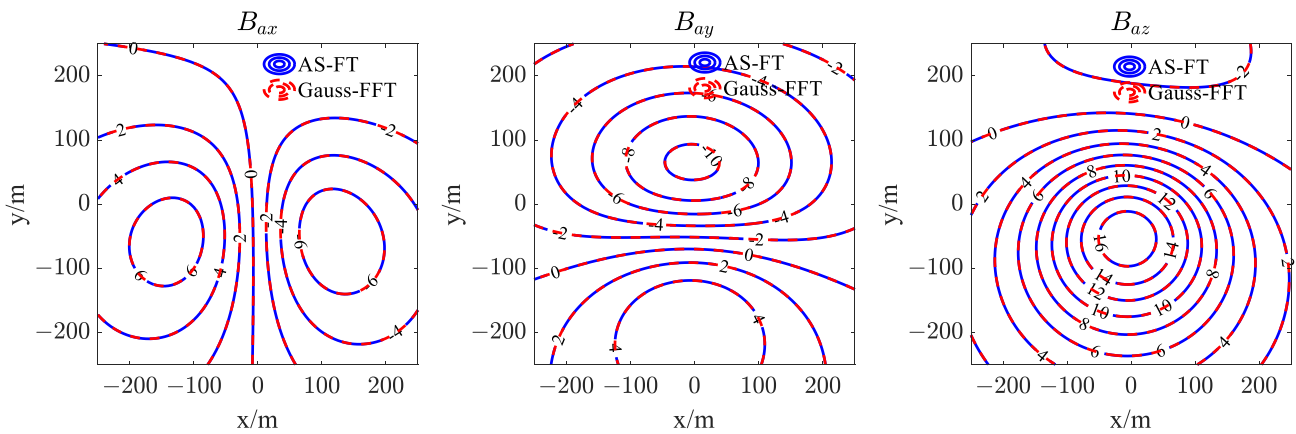


Figure 13. Comparison between weak magnetic sphere model and analytical solution ($z = 0$ m).

5.3.3. Strong Magnetic Catastrophe Medium

We continued to use the sphere model in Figure 10 and set the magnetic susceptibility of the sphere to 1 SI. The other model parameters were consistent with those in Section 5.3.2. It can be seen that the model is under strong magnetic conditions.

The spectrum distribution of the anomaly field at different depths of the model is shown in Figure 14. Similarly, we analyzed the spectrum distribution of $z = 0$ m, 100 m, 200 m, and 250 m planes. Compared with the weak magnetic spectrum distribution in Figure 11, the energy of the strong magnetic spectrum is enhanced by two orders of magnitude, but the spectrum's shape is the same; it is also oscillatory, and it is attenuated to zero at the cut-off frequency.

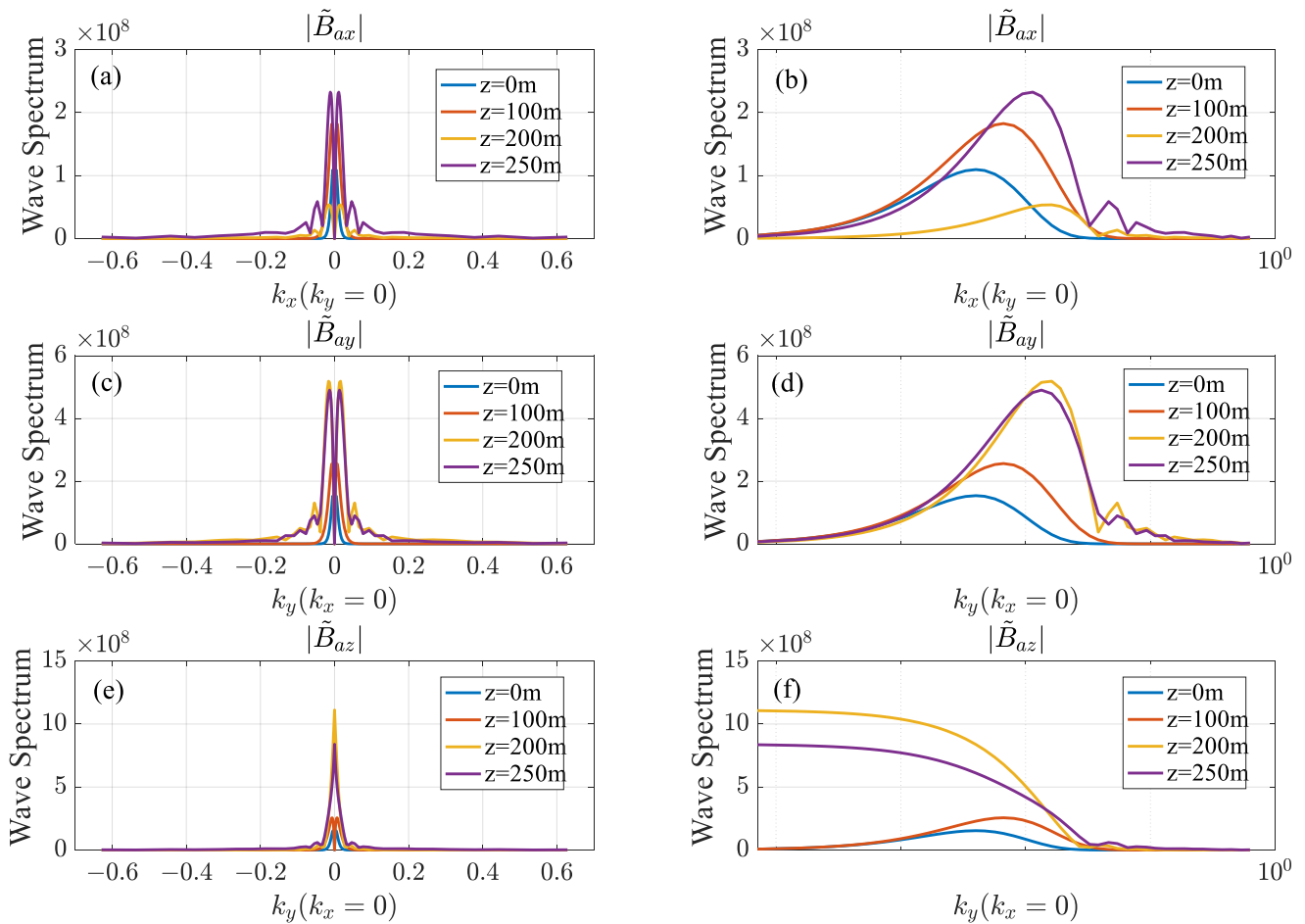


Figure 14. Spectrum distribution of strong magnetic field at different depths. The horizontal ordinate of figures (a,c,e) is non-logarithmic, and the horizontal ordinate of figures (b,d,f) is logarithmic.

To understand the 3D distribution of the spectrum, the distribution of the magnetic anomaly spectrum at the position of $z = 250$ m is shown in Figure 15. The strong magnetic catastrophe model spectrum is concentrated according to the spectrum's distribution. Still, the oscillation is intense, the energy is strong, and the attenuation is slow. There is still strong energy at large wavenumbers, which cannot be ignored. Therefore, to ensure accuracy, it is necessary to expand the wavenumber selection range to $-0.25-0.25$.

After determining the wavenumber selection interval, we changed the spatial domain and wavenumber domain sample methods. The accuracy of numerical simulation under different division methods is shown in Table 5. The number of sample nodes was $N_x = N_y = N_z = 101$, and $N_{kx} = N_{ky} = 101$, respectively.

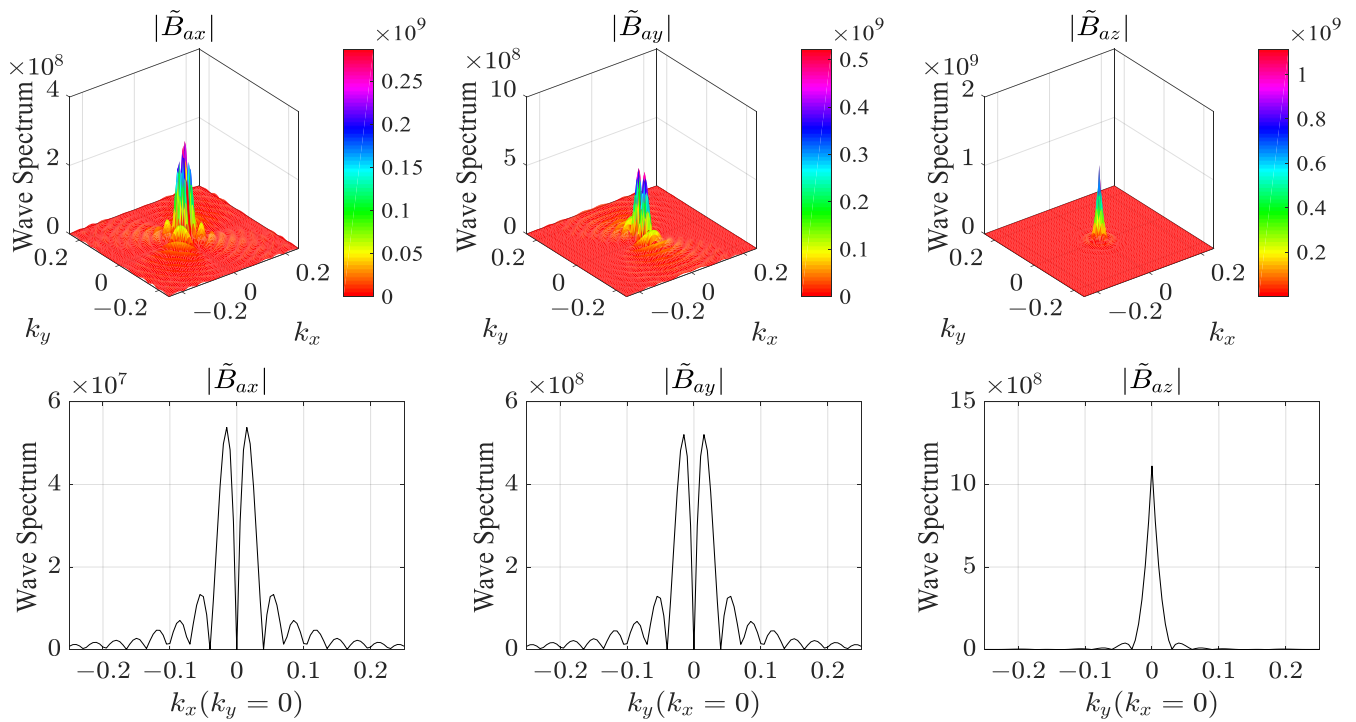


Figure 15. Spectral distribution of strong magnetic field in wavenumber domain ($z = 250$ m).

Table 5. Accuracy statistics of different sampling points between -0.25 and 0.25 in the wavenumber domain ($z = 0$ m, $N_x = N_y = N_z = 101$, $N_{kx} = N_{ky} = 101$).

Sampling Methods		Rrms Error (%)		
Spatial Domain	Wavenumber Domain	B_{ax}	B_{ay}	B_{az}
Uniform	Uniform	1.91	1.82	1.83
Uniform	Log-domain uniform	0.95	1.08	0.95
Non-uniform	Piecewise uniform	0.19	0.24	0.25
Non-uniform	Log-domain uniform	0.17	0.17	0.21

It can be seen from Table 5 that in the case of uniform sampling in both the space and the wavenumber domain, the Rrms errors of B_{ax} , B_{ay} , B_{az} are 1.91%, 1.82%, and 1.83%, respectively. In the case of uniform sampling in the spatial domain and logarithmic sampling in the wavenumber domain the Rrms errors of B_{ax} , B_{ay} , B_{az} are 0.95%, 1.08%, and 0.95%, respectively.

Next, to better fit the abnormal body, non-uniform sampling was selected in the spatial domain. The spatial domain was divided non-uniformly in the horizontal direction, and the sample was densified at the abnormal sphere. The sample interval away from the abnormal sphere was gradually increased, with the minimum grid spacing of 1 m and the maximum grid spacing of 32 m. Its grid is shown in Figure 16a. Piecewise uniform and log-domain sampling were adopted for the wavenumber range of $-0.25-0.25$. The strategy of piecewise uniform sampling is to divide into three segments according to the spectral energy distribution, with uniform sampling in each part. Taking the positive wavenumber as an example, 31 nodes were taken from 0 to 0.04, 11 nodes were taken from 0.04 to 0.1, and 11 nodes were taken from 0.1 to 0.25. The negative wavenumber was symmetrical with the positive wavenumber, with a total of 101 nodes, as shown in Figure 16b. When piecewise uniform sampling was adopted, after six iterations, the Rrms errors of the numerical solution of the ground field value B_{ax} , B_{ay} , B_{az} were 0.19%, 0.24%, and 0.25% compared with the analytical solution of the strong magnetic sphere, respectively. When piecewise uniform sampling was adopted, after six iterations, the Rrms errors of the numerical solution of the ground field value B_{ax} , B_{ay} , B_{az} were 0.17%,

0.17%, and 0.21%, respectively. Therefore, high accuracy can be achieved in the cases of non-uniform sampling in the spatial domain, piecewise uniform sampling, and log-domain sampling in the wavenumber domain. This shows that the AS-FT algorithm can realize arbitrary samples and has high computational efficiency and accuracy.

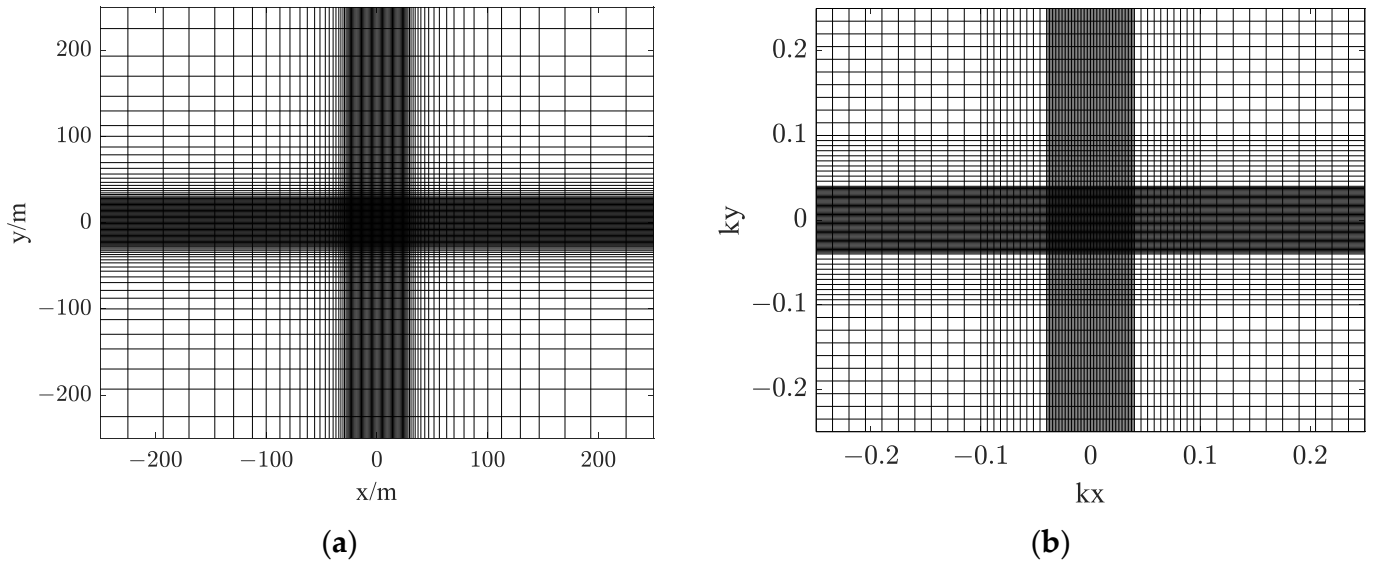


Figure 16. Schematic diagram of horizontal non-uniform sectioning. (a) Spatial domain sample, (b) Wavenumber domain sample.

The comparison between the numerical simulation results and analytical solutions of the non-uniform sample in the spatial domain and log-domain sample in the wavenumber domain is shown in Figure 17. The isolines of the two solutions in the figure are consistent, indicating that AS-FT is still very suitable for strong magnetic models.

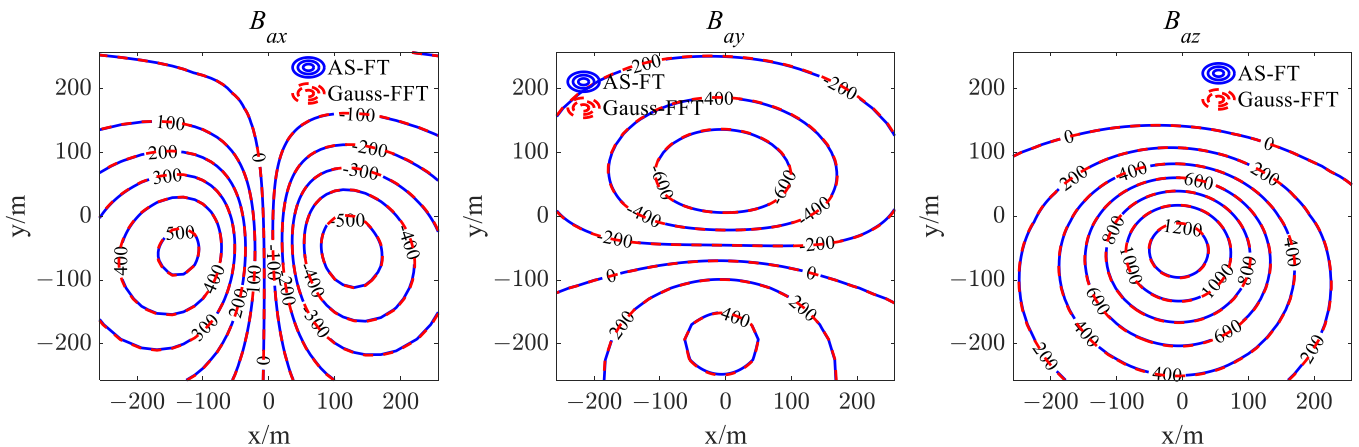


Figure 17. Comparison between numerical solutions and analytical solutions of strong magnetic sphere.

Based on the AS-FT algorithm, the 3D numerical simulation of the weak and strong magnetic field in the space-wavenumber domain has excellent performance. The AS-FT can obtain high-precision solutions and higher computational efficiency in fewer wavenumbers than Gauss-FFT and standard-FFT. Compared with the catastrophe model oscillates in the spectrum, and the spectrum distribution range is broader. Still, the simple selection of wavenumbers can also calculate the model accurately. The spectrum’s energy is enhanced from a weak magnetic to a strong magnetic field, and the calculation accuracy can still be guaranteed by expanding the wavenumber selection interval. The energy distribution of the strong magnetic catastrophe model is the most complex, the

spectrum amplitude is the largest, the oscillation is violent, and the selection of wavenumber is more complex, but a high-precision solution is obtained by non-uniform sampling. In conclusion, AS-FT has good adaptability to the 3D numerical simulation of weak and strong magnetic fields.

6. Discussion

In the field of exploration geophysics, the solution of partial differential equations is one of the most important topics. However, most current algorithms for solving partial differential equations cannot consider accuracy and efficiency, so it is necessary to propose an efficient and high-precision solution. In this paper, we propose an arbitrary sampling Fourier transform algorithm based on quadratic interpolation of the shape function. After combining the AS-FT algorithm and the spatial wavenumber domain algorithm, we applied them to the magnetic method numerical simulation to achieve high-efficiency and high-accuracy imaging of the magnetic field [33].

We compared AS-FT, standard-FFT, and Gauss-FFT with the space-wavenumber domain algorithm to realize magnetic field numerical simulation.

Numerical simulation based on standard-FFT and Gauss-FFT does not require wavenumber selection, and the simulation process is relatively simple [24,26,33]. The AS-FT algorithm in this paper can achieve high-precision simulation only when the wavenumber is selected accurately. However, the process is relatively simple and greatly improves the algorithm's efficiency, which is very valuable for research.

Numerical simulation based on standard-FFT has a strong edge effect, and it often requires edge expanding to reduce the edge effect and improve the calculation accuracy. Still, the edge expanding constantly sacrifices calculation efficiency [33]. Numerical simulation based on Gauss-FFT weakens the influence of the edge effect, but it demands more memory with lower efficiency [33]. However, the numerical simulation based on AS-FT has almost no edge effect. The computational efficiency is superior to the standard-FFT and Gauss-FFT, and it can therefore achieve high-efficiency and high-precision numerical simulation research.

Numerical simulation based on standard-FFT and Gauss-FFT can only achieve uniform sampling. In contrast, numerical simulation based on the AS-FT algorithm can achieve non-uniform sampling, so it can flexibly sample according to the sampling requirements, and achieve the highest accuracy with the fewest sampling points.

Therefore, the AS-FT algorithm based on shape function interpolation proposed in this paper provides an efficient and high-precision method of solving partial differential equations. This algorithm does not need to expand the edge, can effectively avoid the influence of edge effects, and can achieve non-uniform sampling. It is significant to the development and perfection of exploration geophysics theory.

7. Conclusions

This paper proposes an arbitrary sampling Fourier transform method (AS-FT) based on quadratic interpolation of shape function. This method calculates the Fourier transform coefficients in advance, flexibly sets the sampling interval according to the distribution of field and spectrum, and can obtain a semi-analytical solution in the integral interval, taking into account both accuracy and efficiency, and there are no edge effects. The correctness and efficiency of the algorithm were verified by Fourier transform pairs. The AS-FT algorithm was applied to the numerical simulation of magnetic anomalies. Compared with standard-FFT and Gauss-FFT under weak magnetic conditions, we showed that the AS-FT algorithm has higher accuracy and efficiency. Under the condition of weak magnetic field and strong magnetic field, it achieved higher accuracy with fewer sampling points, which shows the high accuracy and efficiency of the AS-FT algorithm. This paper only mentions the application of the AS-FT algorithm to magnetic anomaly simulation. It could also be applied to gravity, electromagnetic, and seismic numerical simulation to further prove the AS-FT algorithm's universality.

Combined with the spatial wavenumber domain theory, the AS-FT algorithm has advantages in solving partial differential equations. The combination can perfectly solve the boundary effect, realize arbitrary sampling in spatial and wavenumber domains, and achieve efficient and high-precision solution of partial differential equations. Therefore, the AS-FT algorithm proposed in this paper provides a new means for solving partial differential equations with high efficiency and accuracy. It has contributed to geophysical forward and inversion research and the improvement of exploration geophysics theory.

Author Contributions: Conceptualization, S.D. and Y.Z.; methodology, S.D. and Y.Z.; validation, S.D., Y.Z., K.L., Q.C. and J.L.; formal analysis, Y.Z.; investigation, Y.Z.; writing—original draft preparation, Y.Z.; writing—review and editing, Y.Z.; visualization, Y.Z.; supervision, S.D.; project administration S.D., Y.Z. and J.L.; funding acquisition, S.D. All authors have read and agreed to the published version of the manuscript.

Funding: This research was funded by the National Natural Science Foundation of China (No. 41574127).

Institutional Review Board Statement: Not applicable.

Informed Consent Statement: Not applicable.

Data Availability Statement: Not applicable.

Acknowledgments: All contributors to this work have been included as authors. We would like to thank the editor and the reviewers for helping us improve the quality of the manuscript.

Conflicts of Interest: The authors declare no conflict of interest.

Appendix A

When the wavenumber k_x is not equal to 0, W_1, W_2, W_3 in the equation are, respectively,

$$\begin{aligned} W_1 &= \frac{1}{(x_1-x_3)^2} [2\int_{x_1}^{x_3} x^2 e^{-ik_x x} dx - (x_1 + 3x_3)\int_{x_1}^{x_3} x e^{-ik_x x} dx + (x_1 + x_3)x_3\int_{x_1}^{x_3} e^{-ik_x x} dx] \\ W_2 &= -\frac{4}{(x_1-x_3)^2} [\int_{x_1}^{x_3} x^2 e^{-ik_x x} dx - (x_1 + x_3)\int_{x_1}^{x_3} x e^{-ik_x x} dx + x_1 x_3 \int_{x_1}^{x_3} e^{-ik_x x} dx] \\ W_3 &= \frac{1}{(x_1-x_3)^2} [2\int_{x_1}^{x_3} x^2 e^{-ik_x x} dx - (3x_1 + x_3)\int_{x_1}^{x_3} x e^{-ik_x x} dx + (x_1 + x_3)x_1\int_{x_1}^{x_3} e^{-ik_x x} dx] \end{aligned} \tag{A1}$$

The integral kernel functions of $W_1, W_2,$ and W_3 both include $x^2 e^{-ik_x x}, x e^{-ik_x x},$ and $e^{-ik_x x}$ and the analytical solution of their element integral on $[x_1, x_3]$ is

$$\begin{aligned} \int_{x_1}^{x_3} x^2 e^{-ik_x x} dx &= -\frac{1}{ik_x} (x_3^2 e^{-ik_x x_3} - x_1^2 e^{-ik_x x_1}) + \frac{2}{k_x^2} (x_3 e^{-ik_x x_3} - x_1 e^{-ik_x x_1}) + \frac{2}{ik_x^3} (e^{-ik_x x_3} - e^{-ik_x x_1}) \\ \int_{x_1}^{x_3} x e^{-ik_x x} dx &= -\frac{1}{ik_x} (x_3 e^{-ik_x x_3} - x_1 e^{-ik_x x_1}) + \frac{1}{k_x^2} (e^{-ik_x x_3} - e^{-ik_x x_1}) \\ \int_{x_1}^{x_3} e^{-ik_x x} dx &= -\frac{1}{ik_x} (e^{-ik_x x_3} - e^{-ik_x x_1}) \end{aligned} \tag{A2}$$

The semi-analytical solutions of W_1, W_2, W_3 can be obtained when k_x is not equal to 0:

$$\begin{aligned} W_1 &= \frac{1}{(x_1-x_3)^2} [\frac{1}{ik_x} (e^{-ik_x x_1} (x_1 - x_3)^2) + \frac{1}{k_x^2} (e^{-ik_x x_3} (x_3 - x_1) + 3e^{-ik_x x_1} (x_3 - x_1)) + \frac{4}{ik_x^3} (e^{-ik_x x_3} - e^{-ik_x x_1})] \\ W_2 &= -\frac{4}{(x_1-x_3)^2} [\frac{1}{k_x^2} (x_3 - x_1) (e^{-ik_x x_3} + e^{-ik_x x_1}) + \frac{2}{ik_x^3} (e^{-ik_x x_3} - e^{-ik_x x_1})] \\ W_3 &= \frac{1}{(x_1-x_3)^2} [-\frac{1}{ik_x} (e^{-ik_x x_3} (x_1 - x_3)^2) + \frac{1}{k_x^2} (e^{-ik_x x_3} (3(x_3 - x_1)) + e^{-ik_x x_1} (x_3 - x_1)) + \frac{4}{ik_x^3} (e^{-ik_x x_3} - e^{-ik_x x_1})] \end{aligned} \tag{A3}$$

References

1. Bhattacharyya, B.K.; Navolio, M.E. A Fast Fourier Transform Method for Rapid Computation of Gravity and Magnetic Anomalies Due to Arbitrary Bodies*. *Geophys. Prospect.* **1976**, *24*, 633–649. [[CrossRef](#)]
2. Chai, Y.P. A-E Equation of Potential Field Transformations in the Wavenumber Domain and Its Application. *Appl. Geophys.* **2009**, *6*, 205–216. [[CrossRef](#)]
3. Boyd, J.P.; Marilyn, T.; Eliot, P. Chebyshev and Fourier Spectral Methods. *Dover Publ.* **2000**, *3*, 1–4. [[CrossRef](#)]
4. Haskell, B. Frame-to-Frame Coding of Television Pictures Using Two-Dimensional Fourier Transforms (Corresp.). *IEEE Trans. Inform. Theory* **1974**, *20*, 119–120. [[CrossRef](#)]

5. Bamberger, R.H.; Smith, M.J.T. A Filter Bank for the Directional Decomposition of Images: Theory and Design. *IEEE Trans. Signal Process.* **1992**, *40*, 882–893. [[CrossRef](#)]
6. Jacquin, A.E. Image Coding Based on a Fractal Theory of Iterated Contractive Image Transformations. *IEEE Trans. Image Process. A Publ. IEEE Signal Process. Soc.* **1992**, *1*, 18–30. [[CrossRef](#)]
7. Cooley, J.W.; Tukey, J.W. An Algorithm for the Machine Calculation of Complex Fourier Series. *Math. Comput.* **1965**, *19*, 297–301. [[CrossRef](#)]
8. Rader, C.M. Discrete Fourier Transforms When the Number of Data Samples Is Prime. *Proc. IEEE* **1968**, *56*, 1107–1108. [[CrossRef](#)]
9. Winograd, S. On Computing the Discrete Fourier Transform. *Proc. Natl. Acad. Sci. USA* **1976**, *73*, 1005–1006. [[CrossRef](#)]
10. Dutt, A.; Rokhlin, V. Fast Fourier Transforms for Nonequispaced Data. *SIAM J. Sci. Comput.* **1993**, *14*, 1368–1393. [[CrossRef](#)]
11. Beylkin, G. On the Fast Fourier Transform of Functions with Singularities. *Appl. Comput. Harmon. Anal.* **1995**, *2*, 363–381. [[CrossRef](#)]
12. Liu, Q.H.; Nguyen, N. An Accurate Algorithm for Nonuniform Fast Fourier Transforms (NUFFT's). *IEEE Microw. Guid. Wave Lett.* **1998**, *8*, 18–20. [[CrossRef](#)]
13. Fessler, J.A.; Sutton, B.P. Nonuniform Fast Fourier Transforms Using Min-Max Interpolation. *IEEE Trans. Signal Process.* **2003**, *51*, 560–574. [[CrossRef](#)]
14. Potts, D.; Steidl, G.; Nieslony, A. Fast Convolution with Radial Kernels at Nonequispaced Knots. *Numer. Math.* **2004**, *98*, 329–351. [[CrossRef](#)]
15. Greengard, L.; Lee, J.Y. Accelerating the Nonuniform Fast Fourier Transform. *SIAM Rev.* **2004**, *46*, 443–454. [[CrossRef](#)]
16. Frigo, M.; Johnson, S.G. The Design and Implementation of FFTW3. *Proc. IEEE* **2005**, *93*, 216–231. [[CrossRef](#)]
17. Lee, J.Y.; Greengard, L. The Type 3 Nonuniform FFT and Its Applications. *J. Comput. Phys.* **2005**, *206*, 1–5. [[CrossRef](#)]
18. Keiner, J.; Kunis, S.; Potts, D. Fast Summation of Radial Functions on the Sphere. *Computing* **2006**, *78*. [[CrossRef](#)]
19. Keiner, J.; Kunis, S.; Potts, D. Using NFFT 3—A Software Library for Various Nonequispaced Fast Fourier Transforms. *ACM Trans. Math. Softw.* **2009**, *36*, 1–30. [[CrossRef](#)]
20. Keiner, J.; Potts, D. Fast Evaluation of Quadrature Formulae on the Sphere. *Math. Comp.* **2008**, *77*, 397–419. [[CrossRef](#)]
21. Barnett, A.H.; Magland, J.F.; Klinteberg, L.A. A Parallel Non-Uniform Fast Fourier Transform Library Based on an “Exponential of Semicircle” Kernel. *SIAM J. Sci. Comput.* **2019**, *41*, C479–C504. [[CrossRef](#)]
22. Caratori Tontini, F.; Cocchi, L.; Carmisciano, C. Rapid 3-D Forward Model of Potential Fields with Application to the Palinuro Seamount Magnetic Anomaly (Southern Tyrrhenian Sea, Italy). *J. Geophys. Res.* **2009**, *114*, B02103. [[CrossRef](#)]
23. Chai, Y.P. Shift Sampling Theory of Fourier Transform Computation. *Sci. China Ser. E Technol. Sci.* **1997**, *40*, 21–27. [[CrossRef](#)]
24. Wu, L.Y.; Tian, G. High-Precision Fourier Forward Modeling of Potential Fields. *Geophysics* **2014**, *79*, G59–G68. [[CrossRef](#)]
25. Wu, L. Efficient Modelling of Gravity Effects Due to Topographic Masses Using the Gauss-FFT Method. *Geophys. J. Int.* **2016**, *205*, 160–178. [[CrossRef](#)]
26. Ouyang, F.; Chen, L.W. Iterative Magnetic Forward Modeling for High Susceptibility Based on Integral Equation and Gauss-Fast Fourier Transform. *Geophysics* **2020**, *85*, J1–J13. [[CrossRef](#)]
27. Fan, Z.; Chen, R.S.; Chen, H.; Ding, D.Z. Weak Form Nonuniform Fast Fourier Transform Method for Solving Volume Integral Equations. *Pier* **2009**, *89*, 275–289. [[CrossRef](#)]
28. Wu, L. Comparison of 3-D Fourier Forward Algorithms for Gravity Modelling of Prismatic Bodies with Polynomial Density Distribution. *Geophys. J. Int.* **2018**, *215*, 1865–1886. [[CrossRef](#)]
29. Zhou, Y.M.; Dai, S.K.; Li, K. Cubic-Spline-Interpolation-Based FFT and Its Application in Forward Modeling of Gravity and Magnetic Fields. *Oil Geophys. Prospect.* **2020**, *54*, 915–922.
30. Wang, X.L.; Liu, J.X.; Dai, S.K.; Guo, R.W.; Li, J.; Fan, P.Y. Fast Numerical Simulation of 2D Gravity Anomaly Based on Nonuniform Fast Fourier Transform in Mixed Space-Wavenumber Domain. *J. Appl. Geophys.* **2021**, *194*, 104465. [[CrossRef](#)]
31. Ouyang, F.; Zhao, J.G.; Dai, S.K.; Chen, L.W.; Wang, S.X. Shape-Function-Based Non-Uniform Fourier Transforms for Seismic Modeling with Irregular Grids. *Geophysics* **2021**, *86*, T165–T178. [[CrossRef](#)]
32. Wang, X.L.; Zhao, D.D.; Liu, J.X.; Zhang, Q.J. Efficient 2D Modeling of Magnetic Anomalies Using NUFFT in the Fourier Domain. *Pure Appl. Geophys.* **2022**, *179*, 2311–2325. [[CrossRef](#)]
33. Dai, S.; Zhao, D.D.; Wang, S.G.; Xiong, B.; Zhang, Q.J.; Li, K.; Chen, L.; Chen, Q. Three-Dimensional Numerical Modeling of Gravity and Magnetic Anomaly in a Mixed Space-Wavenumber Domain. *Geophysics* **2019**, *84*, G41–G54. [[CrossRef](#)]
34. Dai, S.K.; Chen, Q.R.; Li, K.; Ling, J. The Forward Modeling of 3D Gravity and Magnetic Potential Fields in Space-Wavenumber Domains Based on an Integral Method. *Geophysics* **2022**, *87*, G83–G96. [[CrossRef](#)]
35. Brigham, E.O.; Morrow, R.E. The Fast Fourier Transform. *IEEE Spectr.* **1967**, *4*, 63–70. [[CrossRef](#)]
36. Zienkiewicz, O.C.; Taylor, R.L.; Zhu, J.Z. *The Finite Element Method: Its Basis and Fundamentals*; Elsevier: Amsterdam, The Netherlands, 2005.
37. Dai, S.K.; Zhao, D.D.; Zhang, Q.J.; Li, K.; Chen, Q.R.; Wang, X.L. Three-Dimensional Numerical Modeling of Gravity Anomalies Based on Poisson Equation in Space-Wavenumber Mixed Domain. *Appl. Geophys.* **2018**, *15*, 513–523. [[CrossRef](#)]
38. Blakely, R.J. *Potential Theory in Gravity and Magnetic Applications*; Cambridge University Press: London, UK, 1996.